Electronic Supplementary Material (ESI) for Energy & Environmental Science.
This journal is © The Royal Society of Chemistry 2020

Electronic Supplementary Information

Tailoring surface wetting states for ultrafast solar-driven water evaporation

*Youhong Guo,[a] Xiao Zhao,[b] Fei Zhao,[a] Zihao Jiao,[b] Xingyi Zhou [a] and Guihua Yu *[a]*

[a] Materials Science and Engineering Program and Department of Mechanical Engineering, The University of Texas at Austin, TX, 78712, USA.

[b] State Key Laboratory of Multiphase Flow in Power Engineering, Xi'an Jiaotong University, Xi'an, Shaanxi 710049, China

* E-mail: ghyu@austin.utexas.edu

Contents

S1. Supplementary Figures and Tables

Table S1. Parameters for full atom models for OTS, PVA and PVA+OTS, where ε and σ are L-J potential parameters.

	ε (kcal·mol^{-1})	σ (Å)	charge (e)
OTS			
1	0.0803	3.5	0
2	0.0502	2.57	0
3	0.1554	3.17	-0.7
PVA			
1	0.0803	3.5	0
2	0.0502	2.57	0
3	0.1554	3.17	-1.1
4	0.0803	3.5	0.3
5	0	0	0.8
OTS+PVA			
1	0.0803	3.5	0
2	0.0502	2.57	0
3	0.1554	3.17	0
4	0.1554	3.17	-1.1
5	0.0803	3.5	0.3
6	0	0	0.8

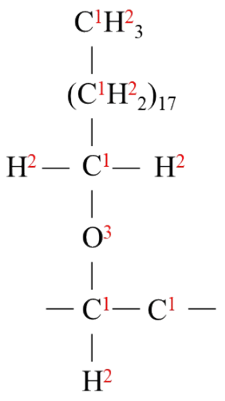

OTS

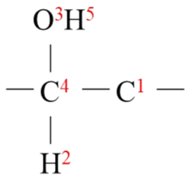

PVA

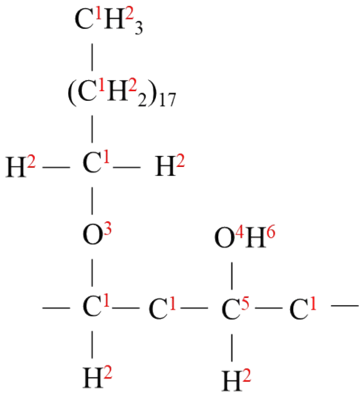

PVA + OTS

S1.1 Microstructure of PSH 30

Fig. S1a shows a cross-sectional SEM image of PSH 30. From the side view of PSH 30, it has a lot of large interconnected channels, which can facilitate rapid replenishment of bulk water to the hydrogel evaporation surface. The pore size of PSH 30 ranges from less than 10 µm to several hundred microns. Fig. S1b shows the internal microporous structure of PSH 30 hydrogel and corresponding energy-dispersive spectroscopy (EDS) mapping images of carbon (Fig. S1c) and titanium (Fig. S1d), indicating a uniform distribution of solar absorber inside hydrogel mesh.

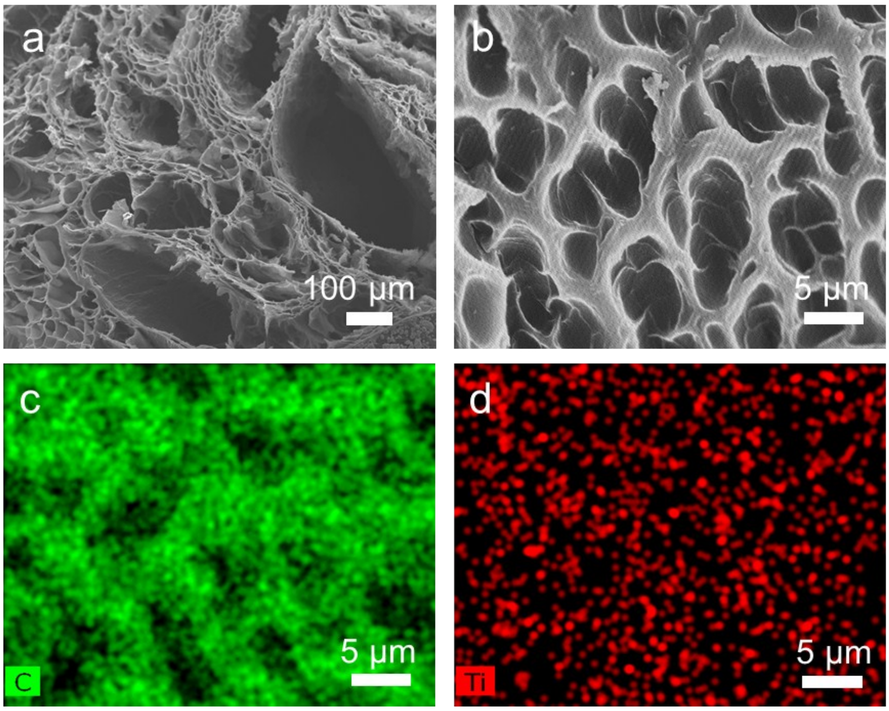

Figure S1. Microstructure of PSH 30. a, cross-sectional SEM image of a sponge-like structure of PSH 30. **b-d**, (**b**) SEM images of internal microporous structure, and corresponding energy-dispersive spectroscopy (EDS) mapping images of carbon (**c**) and titanium (**d**) elements of PSH 30.

S1.2 Characterization of solar absorber

The solar absorbers, Ti_2O_3 nanoparticles, were obtained by high-energy ball-milling process. The diameter of the particles is from 50 to 300 nanometers (inset in Fig. S2). The X-ray diffraction pattern of the as-synthesized Ti_2O_3 nanoparticles was well indexed by JCPDS 10-0063, confirming their corundum phase (Fig. S2).

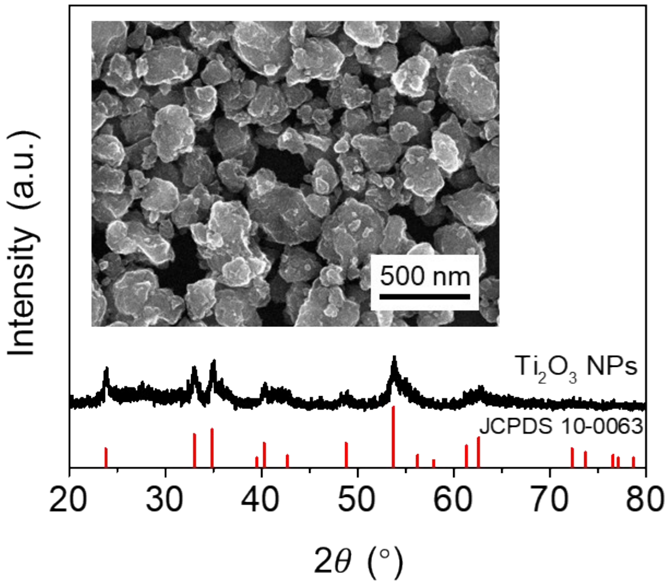

Figure S2. X-ray powder diffraction pattern of the as-synthesized solar absorber, Ti_2O_3 nanoparticles. Inset: SEM image pf as-fabricated Ti_2O_3 nanoparticles.

S1.3 Optical images of PSH 30.

Fig. S3 shows the surface modification of PSH 30 at both micro- and nano-scale, which permits elongated contact lines.

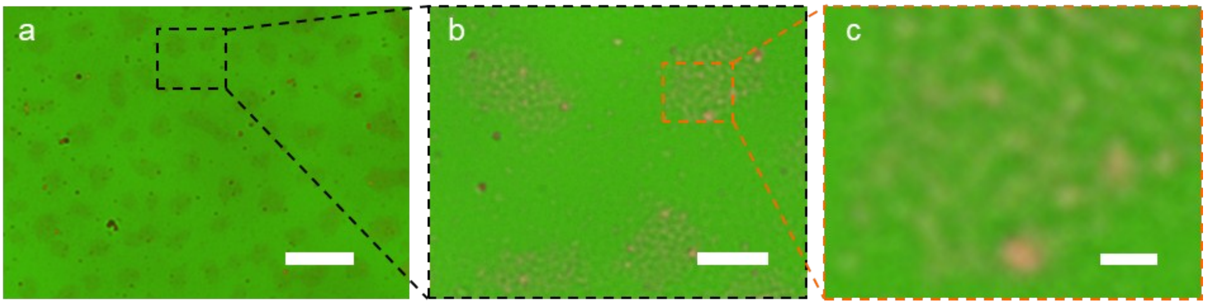

Figure S3. Optical images of PSH 30 surface. a, Micro-scaled OTS islands. Scale bar: 20 µm. **b**, Enlarged area in (**a**) Scale bar: 5 µm. **c**, Nano-scaled OTS islands. Scale bar: 1 µm.

S1.4 Optical profilometer mapping of outmost surface profiles of PSHs

Fig. S4 presents the profilometer mapping of the outmost surface topography of as-synthesized PSHs. The 2D color contour map of PSH 0 shows a very uniform green color, indicating a nearly perfect flat surface of unmodified PVA (Fig. S4a). PSH 30 shows many patches in red color along with an increase in surface roughness (Fig. S4b). As the patches expand, the surface roughness gradually reduces from lightly patched (Fig. S4c) to flat profile (Fig. S4d) with a decrease in RMS roughness (Table S2).

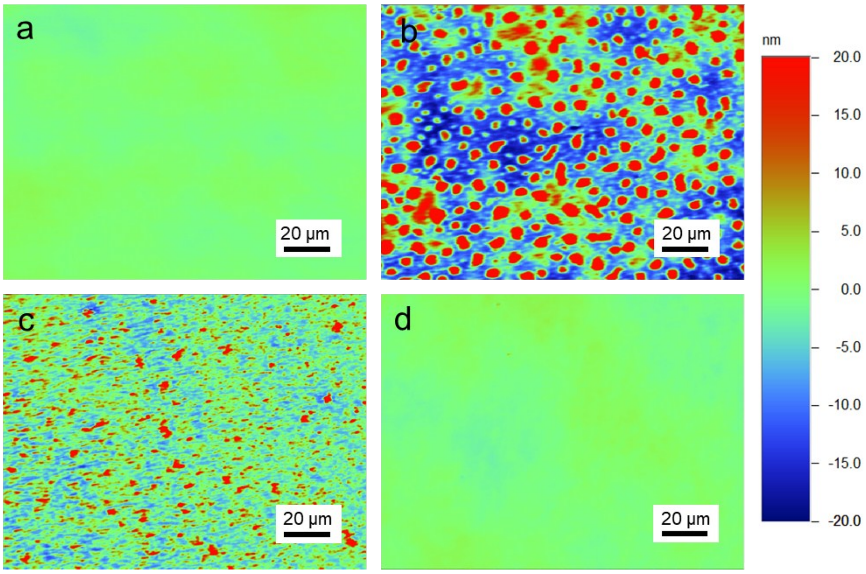

Figure S4. Optical profilometer mapping of the outmost surface layer of as-prepared PSHs. a, PSH 0, **b**, PSH 30, **c**, PSH 60, **d**, PSH 90.

Table S2. RMS roughness and coverage of PSHs.

Soaking time (min)	0	~10	~30	~120
OTS surface coverage (%)	0	30	60	90
RMS roughness (nm) by optical profilometer	0.99 ± 0.18	20.75 ± 5.91	4.70 ± 0.55	0.72 ± 0.16
RMS roughness (nm) by AFM	1.06 ± 0.58	19.55 ± 0.61	4.06 ± 0.46	1.77 ± 0.47

S1.5 Atomic force microscope (AFM) mapping of outmost surface profiles of PSHs

Fig. S5a-d shows the AFM mapping of the outmost surface of PSHs on silicon wafers and the corresponding height profiles Fig. S5e-h of PSH 0, 30, 60, and 90, respectively. The RMS roughness of PSHs measured by AFM is shown in Table S2, which consistent with the values obtained by an optical profilometer.

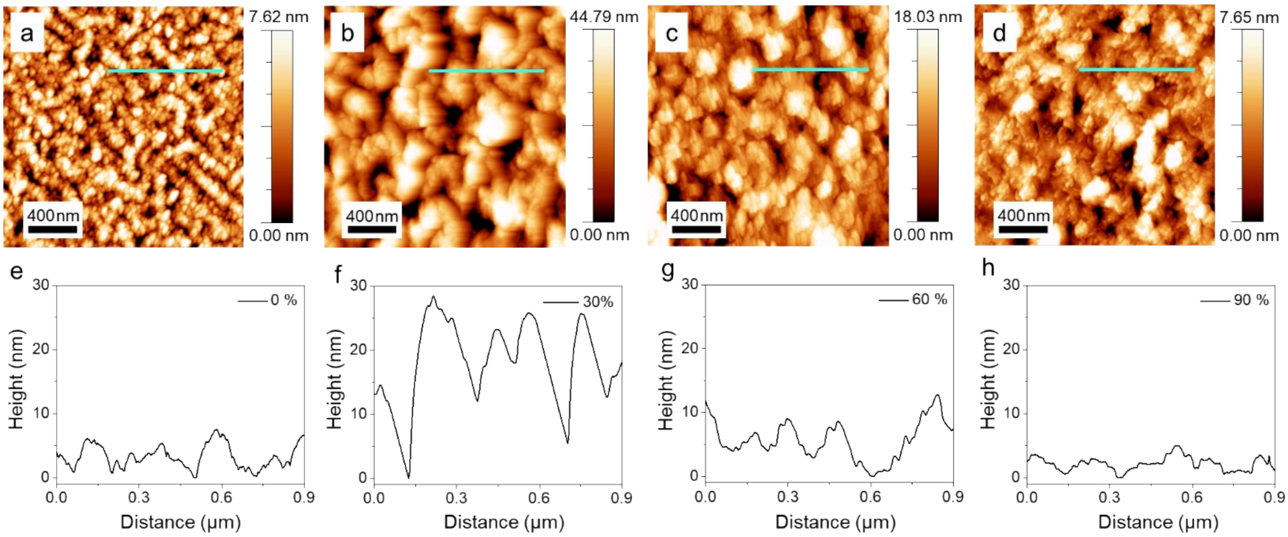

Figure S5. Atomic force microscope mappings of the outmost surface layer of PSHs on silicon wafers. a-d, AFM mapping profiles of PSH 0, PSH 30, PSH 60, and PSH 90, respectively. **e-h,** The corresponding marked vertical height profiles in (**a-d**), respectively.

S1.6 Characterization of surface modification of PSHs

To verify that the modification method (see Supplementary Information S1.2) was mostly limited on the surface instead of affecting the entire structure of the polymeric network of the hydrogel, the compression tests of pure PVA hydrogel, PSH 0, PSH 30, PSH 60 and PSH 90 were carried out. Pure PVA hydrogel presents a fracture strain of ~53% occurred with the stress of ~0.08 MPa (Fig. S6a), which is equivalent to the published results.[1,2] Fig. S6b shows the stress-strain curves of PSHs, when the strain is at 5.5%, PSHs all have similar maximum stress at about ~2.6 MPa, which is about 30 times higher mechanical strength than the pure PVA's, displaying sponge-like structures.[3] The mechanical properties of PSHs confirmed that OTS surface modification did not change the network structure of hydrogels. The inset SEM images are the cross-section of pure PVA hydrogel and PSHs, respectively, and PSHs have a lot larger internal porous structure. The pore size of PSHs is range from less than 10 um to several hundred microns.

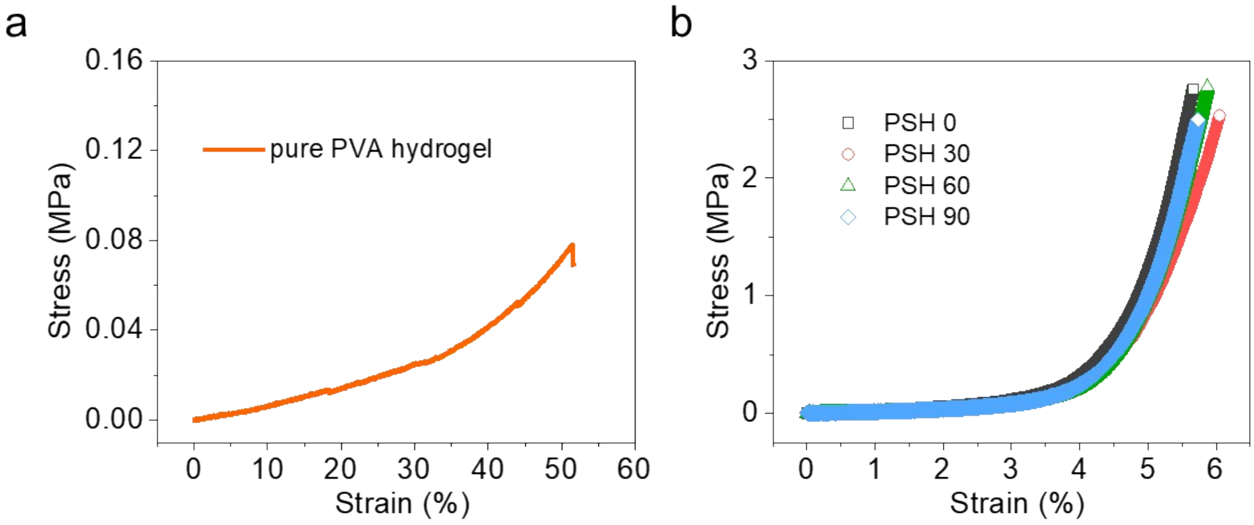

Figure S6. a, Stress-strain curves of pure PVA hydrogel. **b**, Stress-strain curves of PSHs.

S1.7 Evaluation of solar absorption and reflectance of PSHs

The transmittance can be ignored with hydrogels thicker than 0.5 cm, and the absorption loss was due to the reflectance only (Fig. S7a). The reflectance of each PSH was measured by a UV–vis–NIR spectrophotometer (Fig. S7b). All PSHs have a low reflectance, which benefits their solar absorption and ultimately energy utilization. PSH 30 shows the lowest reflectance ($\leq$ 2%) in a wide wavelength range from 400 to 2100 nm due to its highest RMS surface roughness (Table S2). In addition, the increased surface roughness of PSH 30 can enhance the vapor germination by its cavity to speed heat removal, which also contributed to accelerate the evaporation process.[4,5] PSH 0, PSH 60 and PSH 90 all have very similar reflectance (~5%).

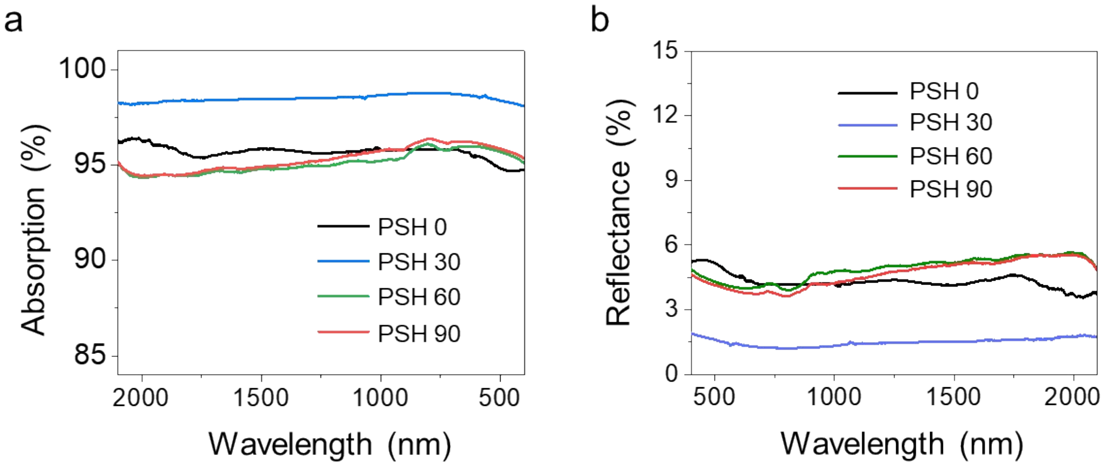

Figure S7. (**a**) Absorption and (**b**) Reflectance spectra of the PSHs in the wavelength range of 400–2100 nm.

S1.8 Equivalent evaporation enthalpy of water in PSHs

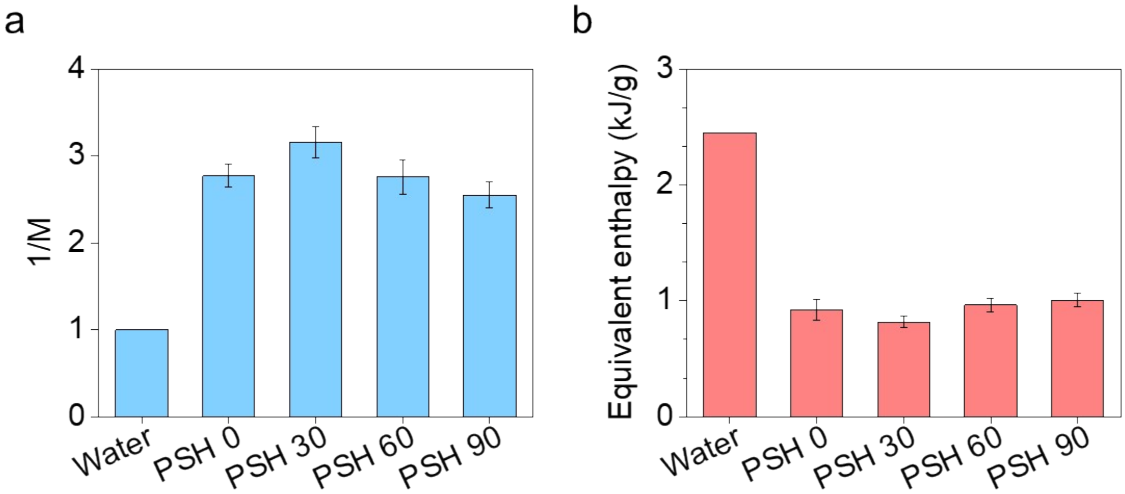

Figure S8. (**a**) Water evaporation rate ratio in dark condition and (**b**) the calculated equivalent enthalpies of water and PSHs.

Previous research has reported that the configuration of water clusters can be varied by polymer networks.[6-8] There are three types of water molecules which are governed by the structure of the polymer network: free water, intermediate water and bound water. The evaporation of intermediate water could be significantly faster than that of the free water as the evaporation enthalpy of water can be reduced.[9] In PSHs, PVA provides lots of -OH groups that form strong hydrogen bonds with water molecules, resulting in water molecules to have weak hydrogen bonds with their surrounding water molecules.[10] These surrounding water molecules are intermediate water, which interacts weakly with polymer chains as well as adjacent water molecules. Hence, forming the intermediate water via the hydrogel polymeric network leads to a reduce energy barrier for evaporation of water.

To estimate the reduced vaporization enthalpy by PSH hydrogel network, a controlled experiment was performed[11]. The water and PSHs with the same surface area were controlled in a closed container at the same time, ambient air pressure and environmental humidity with desiccant. The water evaporation rate ratio and the corresponding calculated E_{equ} are shown in Fig. S8a and b, respectively. The results are equivalent to our previous experiments and DSC measurements.[12] The actual evaporation enthalpy (E_{equ}) of water in PSHs can be estimated by vaporizing the water with identical power input (U_{in}), which has

$$U_{in} = E_0 \times M = E_{equ}$$

where E_0 is the evaporation enthalpy of bulk water and M is the ratio of mass change of bulk water over the mass change of PSHs. The energy efficiency in Fig. 3d was also calculated based on E_{equ} of corresponding PSHs samples.

S1.9 Crystalline antifouling function of PSH 30

Hydrogels have an intrinsic anti-salt-fouling ability when an equilibrium reached by water transport induced salt ion absorption and diffusion enabled salt ion discharge.[13] PSH 30 samples were used for 48 hours of continuous desalination under 1 sun irradiation. A sample was taken out and immersed into deionized water to release the accumulated salt ions. Then, the salt concentrations of washed water samples were tested using inductively coupled plasma spectroscopy (ICP-OSE) to represent the salt ion accumulation in PSH 30 after 1 h, 6 h, 12 h, 24 h and 48 h desalination. Fig. S9 shows that the concentrations of four primary ions is within the same order, almost constant during the continuous test. The insufficient ion accumulation is hard to form crystals, indicating the crystalline antifouling function of PSH 30.

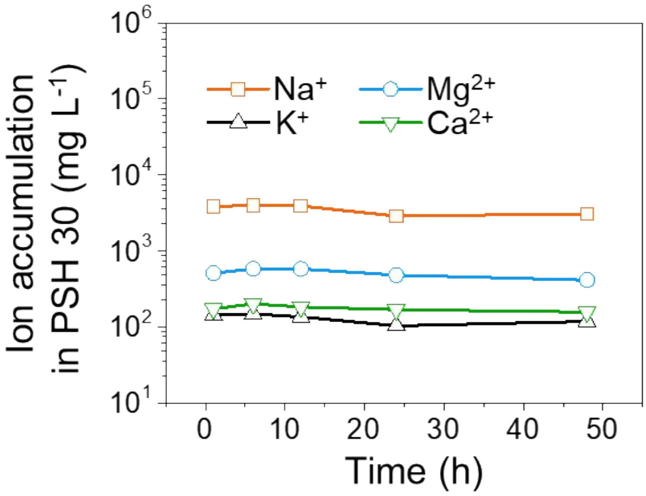

Figure S9. Evaluated concentrations of four primary ions accumulated in PSH 30 over time.

S1.10 Interaction energy of each PSH

As shown in Fig. S10, when the thickness of the water film increases as the hydrophobic area increases from 0% to 90%, the interaction energy between water molecules slightly strengthens, while the interaction energy between water and surface weakens notably. The energy barrier to prevent the evaporation of the water molecule is denoted as the average total interaction energy (e.g., electrostatic interaction, van der Waals interaction) of the outmost water molecule, which is simulated as the sum of the interaction energy between water molecules and interaction energy between water and surface.

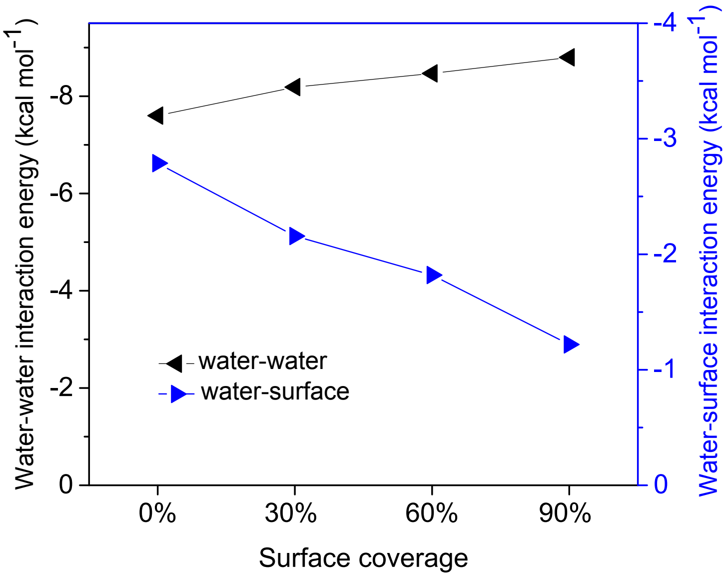

Figure S10, Calculated interaction energy of outmost water molecules in PSHs during evaporation process.

S1.11 Thickness mapping of water film of PSHs

In Fig. S11, the 2D mapping of water molecules on each PSH surface shows increased thickness of water film in the PVA region from PSH 0 to PSH 90. In PSH 30, PSH 60 and PSH 90, water molecules are diffused from hydrophilic region to hydrophobic regions near their contact lines, showing as the white and red dots at the margin and inside of the blue squares. As the contact line increases, the evaporated water contributed from hydrophobic regions increases (Fig. 4f).

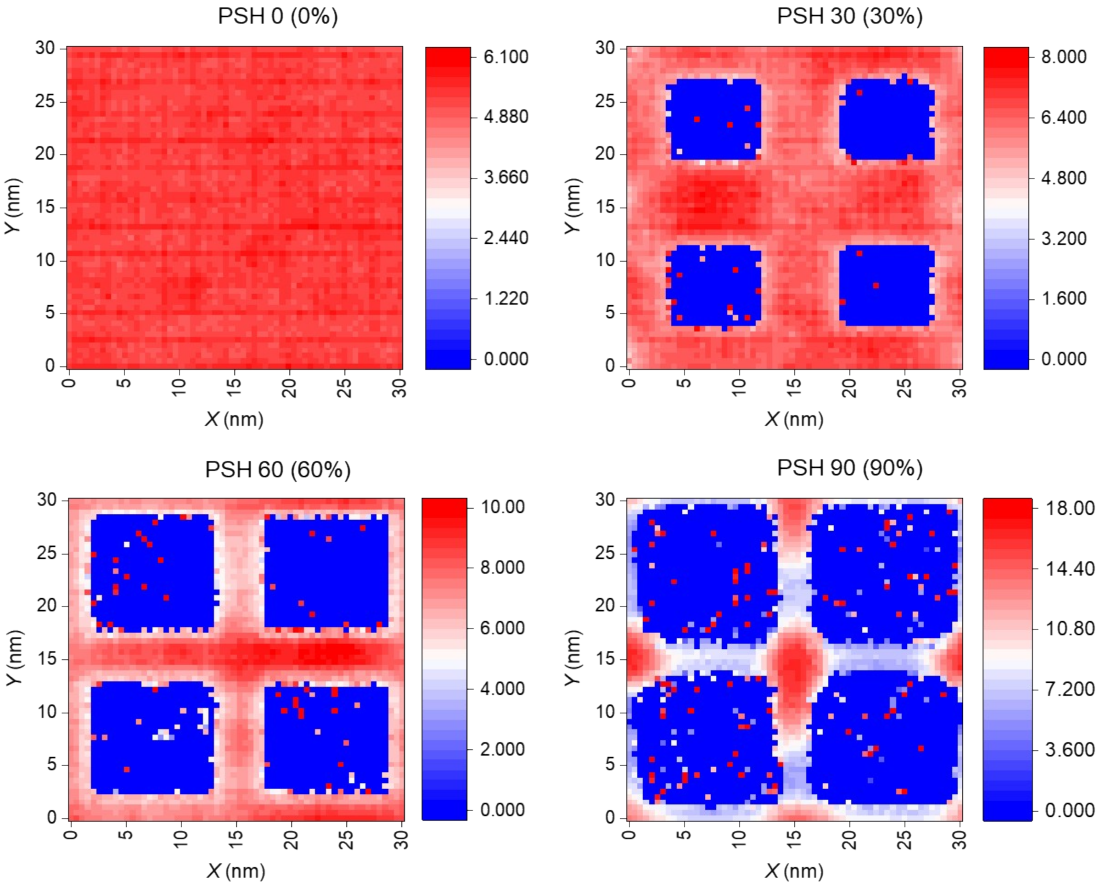

Figure S11, Molecular dynamics summarized 2D mapping of the water film of each PSH, showing both the distribution of water molecules and the thickness of water film.

S1.12 Total contact line length and the contribution from the hydrophobic region

Figure S12 shows the relationship between the total contact line length and water molecules evaporated from the hydrophobic regions. As the area of the hydrophobic region increases, the total length of the contact line is increasing (Figure S11 and S12). By plotting the length of the contact line with the number of water molecules evaporated from the hydrophobic area (Figure 4f), it is clear that they are in the same trend as expected.

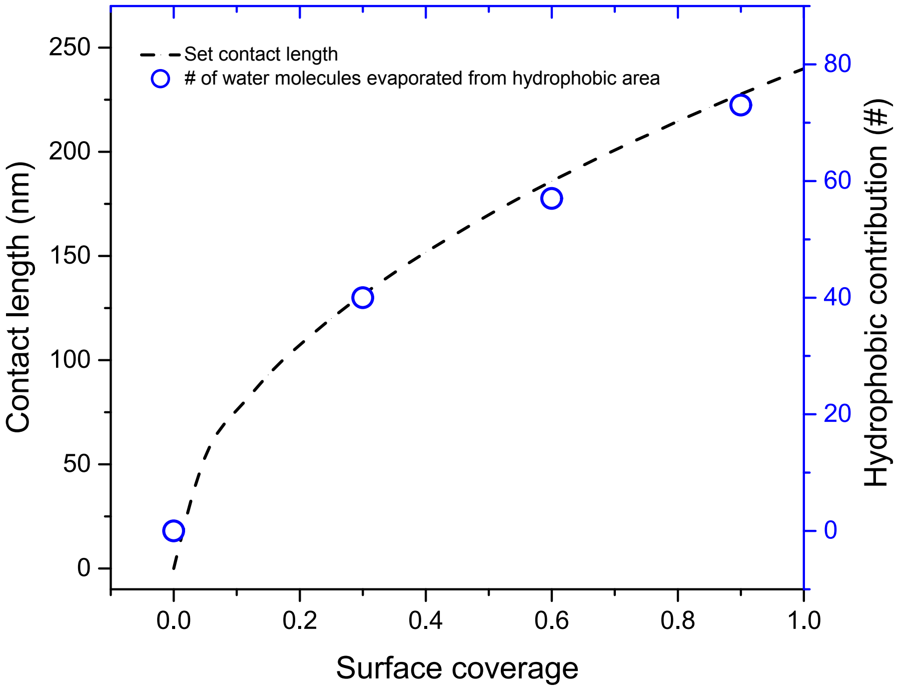

Figure S12. The number of water molecules evaporated from the hydrophobic region is in the same trend with the total length of hydrophilic-hydrophobic contact lines.

S1.13 Schematic illustration of water distribution on PSHs

The water distribution on PSH during the water evaporation process is schematically presented in Fig. S13. A large portion of water molecules is confined in the hydrophilic region, while some water molecules cross the hydrophilic/hydrophobic border and diffuse to the hydrophobic region. The nanoscale OTS islands (Fig. S3) provide elongated water contact lines, allowing more water molecules to diffuse to the hydrophobic region (Fig. S13a). During the evaporation process, a thicker water layer is formed on the hydrophilic region to reduce the electrostatic interaction and van der Waals interaction between the outmost water molecules and the surface of the substrate, thus enhancing the evaporation flux sharply.[14,15] Meanwhile, the diffused water molecules evaporate from the area near the elongated contact lines, contributing to the overall water evaporation process (Fig. S13b). In our PSH with 30% OTS coverage, the water confinement and relatively large hydrophilic area permit rapid water evaporation from the hydrophilic region, and the nanoscale elongated contact lines allow considerable water molecules to evaporate from the hydrophobic region, leading to an ultrafast evaporation rate.

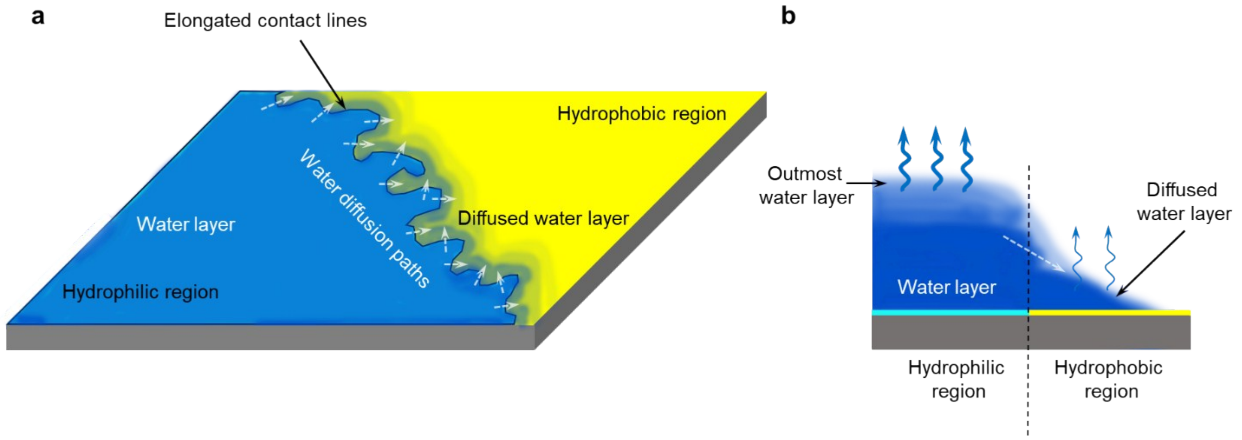

Figure S13 a, Schematic showing the water distribution on PSH surface. **b**, Side-view of (**a**) showing the water evaporation from PSH.

S1.14 Outdoor demonstration and evaluation of water quality

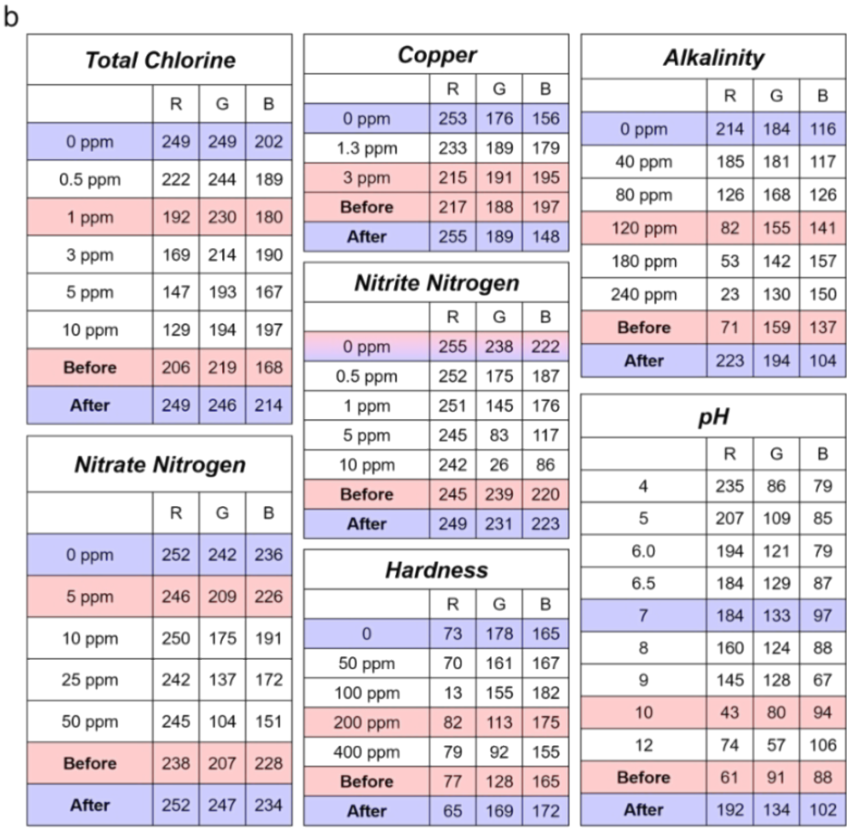

Total Chlorine

	R	G	B
0 ppm	249	249	202
0.5 ppm	222	244	189
1 ppm	192	230	180
3 ppm	169	214	190
5 ppm	147	193	167
10 ppm	129	194	197
Before	206	219	168
After	249	246	214

Nitrate Nitrogen

	R	G	B
0 ppm	252	242	236
5 ppm	246	209	226
10 ppm	250	175	191
25 ppm	242	137	172
50 ppm	245	104	151
Before	238	207	228
After	252	247	234

Copper

	R	G	B
0 ppm	253	176	156
1.3 ppm	233	189	179
3 ppm	215	191	195
Before	217	188	197
After	255	189	148

Nitrite Nitrogen

	R	G	B
0 ppm	255	238	222
0.5 ppm	252	175	187
1 ppm	251	145	176
5 ppm	245	83	117
10 ppm	242	26	86
Before	245	239	220
After	249	231	223

Hardness

	R	G	B
0	73	178	165
50 ppm	70	161	167
100 ppm	13	155	182
200 ppm	82	113	175
400 ppm	79	92	155
Before	77	128	165
After	65	169	172

Alkalinity

	R	G	B
0 ppm	214	184	116
40 ppm	185	181	117
80 ppm	126	168	126
120 ppm	82	155	141
180 ppm	53	142	157
240 ppm	23	130	150
Before	71	159	137
After	223	194	104

pH

	R	G	B
4	235	86	79
5	207	109	85
6.0	194	121	79
6.5	184	129	87
7	184	133	97
8	160	124	88
9	145	128	67
10	43	80	94
12	74	57	106
Before	61	91	88
After	192	134	102

Figure S14. a, Demonstration of the portable and easy-to-carry device. **b**, RGB color analysis of testing kits of creek water and purified water. **c**, Water samples before and after solar vapor generation using PSH 30.

Table S3. Comparison of collected water with several standards

	Total dissolved solids (TDS) (mg/L)	**Conductivity (µs/cm)**
Before SVG (raw creek sample)	651	1100
After SVG (using PSH30 evaporator)	**35**	**60**
Domestic tap water	128	254
Deionized water in the laboratory	4	7
World Health Organization (WHO)	500	/
U.S. Environmental Protection Agency (EPA)	500	/

The main chamber of solar purification jug is 3D printed resin, and the top condenser is made from transparent glass. The weight of solar purification jug is ~0.5 kg, which is easy to carry for outdoor rescue uses (Fig. S14a). The water sample from Waller Creek in Austin, Texas, was used to demonstrate the decontamination ability of PSHs. RGB color analysis was used to determine and confirm the water quality results in each category (Fig. S14b). Total chlorine was reduced from ~1 ppm to ~0 ppm. Copper in creek water sample was reduced from ~3 ppm to ~0 ppm. The alkalinity of creek water was lowered from ~120 ppm to ~0 ppm, and nitrate nitrogen was reduced from ~5 ppm to ~0 ppm. In addition, hardness was improved from ~200 ppm to ~0 ppm, and the pH down from basic to normal after SVG process using PSHs. Nitrite nitrogen in creek water was organically very little so that industrial wastewater could be even better to represent the ability of SVG. The creek water before was quite yellowish with many solid particles, and after SVG using PSHs the water collected was clear without visible solids (Fig. S14c). Total dissolved solids (TDS) and conductivity were significantly lowered even compared to the values of domestic tap water (Table S3), showing PSHs a great potential of decontamination from creek water.

S2. Supplementary References

1 A. Joshi, G. Fussell, J. Thomas, A. Hsuan, A. Lowman, A. Karduna, E. Vresilovic and M. Marcolongo, *Biomaterials*, 2006, **27**, 176-184.

2 H. S. Mansur and H. S. Costa, *Chem. Eng. J.*, 2008, **137**, 72-83.

3 L. Wu, G. Mao, G. Nian, Y. Xiang, J. Qian and S. Qu. *Soft Matter*, 2018, **14**, 4355-4363.

4 Y. Guo, F. Zhao, X. Zhou, Z. Chen and G. Yu, *Nano Lett.*, 2019, **19**, 2530-2536.

5 M.R. Pais, L.C. Chow and E.T. Mahefkey, *J. Heat Transfer*, 1992, **114**, 211-219.

6 Y. Sekine and T. Ikeda-Fukazawa, *J. Chem. Phys.*, 2009, **130,** 034501.

7 M. Miyazaki, A. Fujii, T. Ebata and N. Mikami. *Science*, 2004, **304**, 1134-1137.

8 M.V. Kirov, G.S. Fanourgakis and S.S. Xantheas, *Chem. Phys. Lett.*, 2008, **461**, 180-188.

9 K. Kudo, J. Ishida, G. Syuu, Y. Sekineb and T. Ikeda-Fukazawa, *J. Chem. Phys.*, 2014. **140**, 044909.

10 X. Zhou, F. Zhao, Y. Guo, B. Rosenberger and G. Yu, *Sci. Adv.*, 2019, **5**, eaaw5484.

11 F. Zhao, X. Zhou, Y. Shi, X. Qian, M. Alexander, X. Zhao, S. Mendez, R. Yang, L. Qu and G. Yu, *Nat. Nanotechnol.*, 2018, **13**, 489-495.

12 Y. Guo, X. Zhou, F. Zhao, J. Bae, B. Rosenberger and G. Yu, *ACS Nano*, 2019, **13**, 7913-7919.

13 X. Zhou, F. Zhao, Y. Guo, Y. Zhang and G. Yu, *Energy Environ. Sci.*, 2018, **11**, 1985-1992.

14 R. Wan and G. Shi, *Phys. Chem. Chem. Phys.*, 2017, **19**, 8843-8847.

15 R. Wan, C. Wang, X. Lei, G. Zhou and H. Fang, *Phys. Rev. Lett.*, 2015, **115**, 195901.